Perspectives on selected alloys in contact with eutectic melts for thermal storage: Nitrates, carbonates and chlorides

Solar Energy 224 (2021) 1210–1221

Contents lists available at ScienceDirect

Solar Energy

journal homepage: www.elsevier.com/locate/solener

Perspectives on selected alloys in contact with eutectic melts for thermal storage: Nitrates, carbonates and chlorides

Esraa Hamdy [a,*], Johanna Nockert Olovsjö [b], Christine Geers [a]

[a] Energy and Materials, Chalmers University of Technology, Gothenburg, Sweden
[b] Kanthal AB, Hallstahammar, Sweden

ARTICLE INFO

Keywords:
Thermal storage
High temperature corrosion
Carbonates
Molten chlorides
Carburization
Laves phase

ABSTRACT

Increasing the operating temperature of molten salt-based concentrated solar power plants is of paramount importance to enable next-generation gas turbines and an overall increase in power conversion efficiency. The issue is how to mitigate the degradation of necessary metallic components in highly corrosive salt environments. In this study, three eutectic salt mixture candidates, nitrates, carbonates, and chlorides, are brought into contact with stainless steel (316H or 304L) and the FeCrAl alloy Kanthal® APMT. The post-exposure analysis is discussed in terms of the overall performance of each alloy as concerns mass change, scale growth, internal attack, and leaching. Significant reduction of corrosion is realised through the ability of Kanthal® APMT to form aluminium oxide species at the surface in contact with alkali nitrates and carbonates. On the other hand, aluminium is leached most efficiently in contact with chlorides, which causes a deeper attack on Kanthal® APMT than alloy 304L.

The overall conclusion is that only by employing a holistic perspective on all individual measurements can a long-term performance estimation be formulated.

1. Introduction

Concentrated solar power (CSP) is an appealing energy source utilising the most abundant energy source, the sun (Caitlin et al., 2019). CSP has evolved into a mature technology over the last decade and contributes to the fossil-free electricity production blend used in many countries. Low-cost thermal energy storage (TES), in other applications also referred to as heat transfer fluid (HTF), offers an extension for electrical power supply beyond sunset in CSP plants (Sarvghad et al., 2018a; Walczak et al., 2018; Mehos et al., 2017). To enable greater efficiency in energy conversion for the next generation of CSP technology, it is necessary to overcome the current temperature limit of 560 °C (Steinmann, 2015), which is the decomposition temperature of the currently used eutectic salt mixture of alkali nitrates, 'Solar Salt', which comprises sodium and potassium nitrates. Redesigning CSP plants for the Brayton cycle technology and utilising supercritical carbon dioxide instead of steam for the gas turbines, requires a minimum operating temperature of 750 °C for the TES (IEA, 2010; Zhao et al., 2017; Ellingham, 1944; Yin et al., 2019; Ho et al., 2016). Increasing the temperature of salt melts also increases their corrosivity towards metallic materials. Significant improvement in the compatibility of container material (tanks/pipes/heat exchangers) and the TES medium is therefore necessary (Sarvghad et al., 2018b; Mehos et al., 2017).

Considerable efforts have been dedicated to characterising the thermophysical properties of different types of TES media (Sarvghad et al., 2018a). While Solar Salt is already widely used, alkali carbonates or chlorides have been identified as TES candidates for the next generation CSP. However, each of these candidates differs in abundance, thermal stability, liquidus range, price, and corrosivity (Sarvghad et al., 2018a; Walczak et al., 2018; Mehos et al., 2017). Corrosivity is an apparent obstacle to enabling the first Brayton cycle operated CSP (Mehos et al., 2017). The corrosion of the materials in contact with the storage medium can lead to a catastrophic failure of an entire CSP plant due to material loss or embrittlement.

Typical high-temperature corrosion phenomena that have been reported in TES tanks are localised corrosion and mechanically assisted corrosion (Walczak et al., 2018). The most common alloys and some recently considered grades of carbon steel, stainless steel, and nickel-based alloys have been evaluated using gravimetric, metallographic, and electrochemical techniques (Goods et al., 1994). Carbon and low-alloy steels were among the first candidates considered for TES components that come in contact with molten salts. In the 1990s, Sandia

* Corresponding author.

https://doi.org/10.1016/j.solener.2021.06.069
Received 28 October 2020; Received in revised form 30 May 2021; Accepted 24 June 2021
Available online 7 July 2021

National Laboratories published a report about the corrosion performance of the low-carbon steel A36, a common type of steel used in construction that come in contact with commercial Solar Salt in current CSP plants (Goods and Bradshaw, 2004). It was found that A36 was covered with a thin adherent oxide scale composed primarily of magnetite at 316 °C and over 7000 h of operation. It was concluded that the impurities found in the commercially available alkali nitrates had no significant effect on the corrosion behaviour of the alloy (Goods and Bradshaw, 2004). However, sensitivity to chloride impurities in the nitrate melt has been found with the low-alloy steel A516 gr. 70. Instead of a protective magnetite layer, a thick hematite scale forms on A516 and spalls frequently, causing rapid metal thickness loss and even local pitting attack (Goods et al., 1994; Bradshaw and Clift, 2010; Liu et al., 2016). The distinction between corrosion testing under static and flow conditions should also be emphasised. Tests in flowing TES media can easily increase corrosion rates by a factor of two (Goods et al., 1994; Bradshaw and Clift, 2010; Liu et al., 2016).

Alloy T22, which is another low-alloy steel, has been selected for use in CSP plants after showing good corrosion behaviour at 390 °C in Solar Salt. However, at 550 °C and after 800 h, the alloy was reported to exhibit 'catastrophic' behaviour due to a severe intergranular attack (Goods et al., 1994). Generally, carbon or low-alloy steels, e.g., alloy A516 gr. 70 or T22, respectively, are recommended for moderate- and low-temperature service, considering the temperature range and impurities in Solar Salt (Goods et al., 1994). Grosu, Y. et *al.* investigated humidity and impurities effects on corrosion behaviour of three alloys, carbon steel A516.Gr70 and stainless steels 304 and 316, in contact with molten HitecXL salt. A516.Gr70 alloy suffered most from humidity, while 304 and 316 alloys showed good corrosion resistance under humid conditions. Despite the very low concentrations of impurities, e.g., Mg, Zn, and Cu in HitecXL salt, it has been reported that the impurities might lower the corrosion resistance of the studied alloys (Grosu et al., 2018). Li, H. *et al.* have also studied the effect of chloride impurity on the corrosion performance of stainless steels 304 and 316L exposed to Solar Salt. Results have shown that the more the chloride content, the lower the corrosion resistance and adherence of the oxide layer for both alloys. Also, stainless steel 316L has shown better corrosion resistance than 304 alloy (Li et al., 2021).

Stepwise enhancing the chromium content, Cheng et al. reported that the corrosion resistance of steel exposed to molten $LiNO_3$–$NaNO_3$–KNO_3 at 550 °C up to 1000 h under nitrogen could be drastically improved by the addition of chromium (9 wt%) (Cheng et al., 2015). An outer $LiFeO_2$ and inner $(Fe,Cr)_3O_4$ scale have been identified (Cheng et al., 2015).

Stainless steels have been tested for higher temperatures and reliability. Most published studies describe the corrosion of stainless steels in contact with Solar Salt. It has generally been concluded that: i) the corrosion resistance of stainless steel alloys is better than that of carbon steels; and ii) corrosion increases with an increase in temperature and exposure time (Goods et al., 1994).

The main corrosion products found on stainless steels in contact with Solar Salt are $FeCrO_4$, Fe_2O_3, and a less dense and less protective outer scale of $NaFeO_2$. Of these products, the formation of Fe-Cr spinels at the alloy-oxide interface renders the rate-limiting step of the corrosion process (Walczak et al., 2018; Bradshaw and Goods, 2001; Fernández et al., 2015b). It has generally been reported that corrosion resistance increases with increasing chromium content in stainless-steel alloys (Fernández et al., 2012; Kruizenga and Gill, 2014); however, it is still inconclusive how the actual amount of chromium affects the composition of an oxide layer. Furthermore, other factors must be considered, such as the nickel and molybdenum content in the alloy chemical composition. However, the addition of molybdenum to alloys exposed to Solar Salt has not shown any effect on the corrosion of stainless-steel grades AISI 316/316L, 317L, and OC-4 with respect to Mo-free alloys (Fernández et al., 2014; Sarvghad et al., 2018a). This paper presents our findings for molybdenum effect on high-temperature corrosion caused by molten chlorides.

Another alloying element that has been found to improve corrosion resistance of alloys in chlorides melt by forming a protective oxide scale is aluminium. Fernandez et al., have conducted a comparative study of alumina-forming, chromia-forming stainless steels, and a low-Cr steel alloy. OC-4, which is an alumina-forming austenitic (AFA) alloy, showed better corrosion resistance in Solar Salt at 390 °C than the 304 stainless steel and T22 steel (Fernández et al., 2014). Also, the relatively high amount of Nb and Ni in OC-4 might have improved the stability of the oxide scale, which led to better corrosion resistance (Yamamoto et al., 2008). Meißner, T. et al. have studied corrosion mitigation by employing three different coatings, a pure Ni, a Cr and a combined Ni and Cr coating, on ferritic-martensitic X20CrMoV12-1 steel. The coated samples has been immersed in molten Solar Salt and tested isothermally at 600 °C for up to 1000 h. Results have revealed that the combined Ni and Cr coating has significantly improved the corrosion resistance of the investigated alloy (Meißner et al., 2021).

Eutectic carbonate and chloride salts have been selected as feasible candidates for higher TES operating temperatures. The corrosion performance of different alloys in contact with those salts has been investigated. Chromia-forming alloys, such as AISI 310 and HR3C, have been tested in Li_2CO_3–K_2CO_3 at 650 °C (Ni et al., 2011) and Li_2CO_3–Na_2CO_3–K_2CO_3 at 700 °C, respectively (de Miguel et al., 2016). These temperatures are still rather low. Results have shown degradation of the protective oxide, which can be explained by the lithiation process. This process has been described as the 'successive formation of different oxides and lithiated phases' (Selman, 1999). In this process, internal stresses may develop leading to crack formation that could contribute to mixed potential several oxidation and lithiation reactions (Tzvetkoff and Kolchakov, 2004). The corrosion behaviour of alloy 310 in a molten carbonate fuel cell (MCFC) has been studied at temperatures <600 °C and >675 °C, and no passive behaviour caused by the formation of porous $LiFe_5O_8$ has been reported (Frangini and Loreti, 2006). The main corrosion products detected during the performance of alloy HR3C exposed to Li_2CO_3–Na_2CO_3–K_2CO_3 for 2000 h, were $LiFeO_2$, $LiCrO_2$, NiO, and $FeCr_2O_4$. These produced a chromium-rich layer at the metal/oxide interface. Degradation was found to be enhanced by the formation of soluble chromates, such as K_2CrO_4 , in early stage of the exposure (de Miguel et al., 2016). These soluble chromates successively leach chromium from the passive scale and the alloy.

Gomez-Vidal et al., have also reported unacceptably high corrosion rates for the stainless steels 310, 321, and 347 exposed to K_2CO_3-Na_2CO_3 at 750 °C (Gomez-Vidal et al., 2016). The overall conclusions of previous studies on chromia-forming stainless steel alloys in carbonate salts have underlined the need to consider alternative alloys or coatings that can be implemented in the next generation of CSP plants. Another study conducted by Fernandez et al. aimed at evaluating the corrosion of AFA alloys; in the study, OC-4 and HR224 grades were exposed to Li_2CO_3–Na_2CO_3–K_2CO_3 at 650 °C for 1000 h (Fernández et al., 2019). Both alloys showed significantly better resistance to the corrosion attack of the salts than chromia-forming alloys (Fernández et al., 2019; Goods et al., 1994). This promising performance was attributed to the multilayer scale structure formed; two layers were identified on OC-4 composed of NiO, alumina (Al_2O_3), and hematite (Fe_2O_3). The oxidation process reached steady state through external oxidation. Alloy HR224, however, showed a more complex structure with three layers composed of NiO and two spinels ($NiFe_2O_4$ and $CrFe_2O_4$) that underwent external oxidation during the isothermal test (Fernández et al., 2019). In a recent study, Prieto et al. designed and built an experimental pilot plant for CSP that operates at a temperature higher than 650 °C; molten carbonates were used as the HTF in this pilot. In This pilot plant investigated other parameters, aspects, and materials compatibility, along with evaluating the corrosion performance of different alloys. Results showed that stainless steel 347 had the poorest corrosion resistance, while Kanthal showed sufficient stability (Prieto et al., 2020).

Eutectic chloride melts pose another potential group of candidates

for the TES medium due to their superior thermal stability. However, chlorides are highly corrosive at high temperature. The stainless steel AISI 316L has shown poor corrosion resistance, with rapid formation and spallation of corrosion products, when exposed to LiCl–KCl (Ravi Shankar et al., 2010). Comparative tests on a low-carbon stainless steel (X2CrNi18–9) and a titanium-stabilised high-carbon stainless steel (X6CrNiTi18–10) in LiCl–KCl–CsCl melt in the range of 400–600 °C for up to 27 h have been conducted. It has been revealed that low carbon steel suffered from faster intergranular attack than high carbon steel 'Chlorination–oxidation' is the term used to describe this behaviour by emphasising the role of oxygen. Unlike stainless steel alloys, a Ni-based superalloy (CMSX-4) has been tested at 800 °C for 3 h and showed almost no signs of corrosion (Hofmeister et al., 2015).

Gomez-Vidal and Tirawat have also studied the corrosion behaviour of the alloys AISI 310 and 347 in NaCl–LiCl at 650 °C and 700 °C. Alloy AISI 310 showed relatively good performance, almost as good as In800H at 650 °C for 800 h, unlike alloy 347. The authors explained this the difference in corrosion performance with the alloys' respective nickel content (Gomez-Vidal and Tirawat, 2016).

High operating temperature TES media are very aggressive to common chromia-forming alloys. Recent studies have tested different alumina-forming (Fe-based or Ni-based) alloys (Fernández et al., 2019; Gomez-Vidal et al., 2017a). Industries processing aggressive chemicals at high-temperatures employed Ni-based alloys instead of stainless steels because of their superior resistance to pitting corrosion and crevice attack. Gomez-Vidal et al., have investigated corrosion mitigation by surface passivation of alumina-forming austenitic (AFA) and ferritic alloys (AFF) (Inconel 702, Haynes 224 and Kanthal® APMT) (Gomez-Vidal et al., 2017a).

The AFA alloys showed promising performance against corrosion attack by $MgCl_2$–KCl in oxygen-containing atmospheres for at least 185 h. The pre-oxidised In702 covered with a relatively thick alumina scale has shown best performance (Gomez-Vidal et al., 2017b).

Ding, W. and Bauer, T. have reviewed and summarised recent developments in an attempt to utilise molten chlorides as HTF/TES and the inherent corrosion challenges faced by metallic components in contact with these salts. Some leading suggestions have been reported, e.g., i) salt purification in conjunction with corrosion mitigation methods; ii) the identification of new materials that can withstand such harsh environments (Ding and Bauer, 2021).

In the present study, performance results and requirements for different eutectic melts at intermediate and high operation temperatures were carefully compared. The corrosion behaviour of alumina-forming Kanthal APMT and chromia-forming 304L and 316H was evaluated in alkali nitrates, carbonates, and chlorides. The carbonate and chloride salt mixtures were selected for their potential use in next generation CSP plants, whereas the nitrate mixture, Solar Salt, is currently used in CSPs and thus acts as a reference environment (Walczak et al., 2018; Mehos et al., 2017). The alloys were challenged at temperatures ~100 °C higher than the operating temperatures of the respective melts for 168 h, 500 h, and 1000 h. Here, the aim is to determine the limiting conditions for conventional alloys facing catastrophic corrosion, pitting, and internal attack causing embrittlement.

2. Experiments

We compared the corrosion results of a stainless steel, 304L or 316H, and one distinct AFF, Kanthal APMT, in three different eutectic melts. Melts were selected based on their potential use in commercial CSP plants. The three melts used were: a mixture of alkali nitrates known as Solar Salt (60 wt% $NaNO_3$- 40 wt% KNO_3), carbonates (32.1 wt% Li_2CO_3 -33.4 wt% Na_2CO_3- 34.5 wt% K_2CO_3), and chlorides (64.41 wt% KCl-35.59% wt% $MgCl_2$). The thermophysical properties of the melts can be found in other studies (Gomez-Vidal et al., 2017b; Li et al., 2014; Vignarooban et al., 2015; Ding et al., 2018a).

2.1. Salt preparation

Eutectic mixtures were produced from the following salts: $NaNO_3$ (Alfa Aesar 99.0%), KNO_3 (Alfa Aesar 99.0%), Li_2CO_3 (VWR chemicals 99.0%), Na_2CO_3 (EMSURE anhydrous, 99.9%), K_2CO_3 (ThermoFisher Scientific 99.8%), KCl (Alfa Aesar 99.0%), and $MgCl_2$ (Alfa Aesar anhydrous 99.0%). Impurities concentrations and chemical compositions of each salt are provided in the supplementary A2).

The salt mixtures were prepared as follows: weighed and mixed to the proper ratio in 100 g batches, thoroughly ground using mortar and pestle, dried at 120 °C in a dry oven for at least 24 h, and finally stored in a desiccator cabinet until further use. Chloride salt mixtures were produced via a purification process under Ar to reduce water content crucial for the corrosion experiment (Phillips et al., 2019; Gomez-Vidal et al., 2017a; Ding and Bauer, 2021), (see detailed salt purification process in supplementary A3).

2.2. Alloy preparation

The nominal compositions of the substrate alloys are shown in Table 1.

Metal coupons of initial measurements 15 × 15 × 2 mm were ground and finally polished to a mirror-like finish with a 1 μm diamond suspension. The polished samples were thoroughly cleaned and dried, then dipped into the salt mixture in alumina crucibles (see supplementary A1).

2.3. Experimental setup

Two setups were used in this study, and different conditions were investigated, as summarised in Table 2. The first setup, a horizontal silica tube furnace for partial immersion experiments was used for the exposures to Solar Salt. The exposures were performed isothermally at 650 ± 5 °C in this setup, with a filtered air at a flow rate of 20 ml/min. The second setup used for complete immersion experiments was a top-loader furnace (model top 60 Nabertherm) purchased and redesigned in the workshop to comply with carbonate and chloride exposures in controlled gas environments. The final system layout for the Nabertherm setup can be found in supplementary A4. The exposures were performed isothermally at 800 ± 5 °C, calibrated at the lowest point of the crucibles, with a gas (Ar or CO_2) flow rate of 50 ml/min for each vessel. Detailed corrosion tests procedure for each setup are provided in supplementary A4. Each exposure was conducted twice.

The main purpose of building the Nabertherm setup was as follows: i) ability to test six coupons in each vessel and providing duplicate samples, with an overall of 12 samples tested at a time, see sketch and photo of the Nabertherm setup in the supplementary data A4. ii) Ability to remove coupons directly from the melts; see supplementary section A5, since an otherwise necessary washing procedure of the solidified melts changes the alloy surface chemistry. These samples are dedicated for cross-section analyses. iii) However, the duplicate samples underwent thorough washing for mass change measurements, as recommended in literature (Bradshaw and Clift, 2010; Gomez-Vidal et al., 2017a; Ding, W., 2019; Fähsing et al., 2018; Soleimani Dorcheh et al., 2016; Gomes et al., 2019; Palacios et al., 2020; Encinas-Sánchez et al., 2019).

Table 1
Nominal alloy compositions.

Alloy	Fe	Ni	Cr	Al	Si	Mn	Mo	Others
316H	balance	11.5	17	X	0.6	1.5	2.1	C 0.05
304L	balance	9.5	18.5	X	0.4	1.3	X	C 0,02
Kanthal® APMT	balance	X	21	5	0.7	0.4	3	Y; C 0,08

Table 2
Experimental parameters, eutectic melting point, and decomposition temperature of the different salt mixtures. * Decomposition temperature varies with atmosphere; it is was found to be 1000 °C, 700 °C and 670 °C in exposures to CO_2, Ar and air (Vignarooban et al., 2015).

Eutectic salt mixture	*i.) Nitrates* (60 wt% $NaNO_3$- 40 wt % KNO_3)	*ii.) Carbonates* (32.1 wt% Li_2CO_3 –33.4 wt% Na_2CO_3- 34.5 wt% K_2CO_3)	*iii.) Chlorides* (65 wt% KCl- 35% wt% $MgCl_2$)
$T_{eutectic}$ (°C)	230 (Mehos et al., 2017)	398 (Wu et al., 2011)	423 (Ding et al., 2019c)
T_{max} (°C)	530–565 (Mehos et al., 2017)	>650* (Vignarooban et al., 2015)	>800 (Ding et al., 2018a) (Ding et al., 2019c)
Gas	filtered air	CO_2	argon
Exposure temperature	650 °C (72 h cyclic refilling of the salt)	800 °C (isothermal) (336 h cyclic refilling of the salt)	800 °C (isothermal) (336 h cyclic refilling of the salt)
Total exposure time	168 & 1000 h	168 & 1000 h	168 & 500 h

2.4. Sample characterisation

Sample surfaces and cross sections were investigated. Unwashed samples were subjected to cross-section investigation. A thin salt film remained on each sample after the residual melt was poured off. Cross-sections of the exposed samples were prepared either by cold embedding in epoxy resin, hot mounting in bakelite, or by broad ion beam (BIB) milling with a Leica TIC 3X instrument. Post-exposure treatment details for the coupons are provided in supplementary A6.

Washed samples were weighed and characterised with scanning electron microscopy (SEM) and energy-dispersive X-ray spectroscopy (EDX) using a JEOL JSM-7800F Prime or Phenom ProX Desktop SEM equipped with an EDX detector. The electron beam used to collect EDX spectra was operated at an accelerating voltage of 15 kV. A Siemens D5000 powder diffractometer with grazing-incidence geometry was used for XRD surface analysis. As it is hard to detect Li with EDX analysis because of the Li low molecular weight, it was important to use XRD to detect the Li-containing corrosion products. It is noteworthy that the rinsing procedure of the sample, as described in supplementary A5, can result in the removal of some corrosion products. Therefore, the results for washed samples should be considered with caution.

3. Results and discussion

A quantitative overview of weight change and corrosion depth data showed a clear distinction between the effects of different salt melts on the stainless steels and Kanthal APMT, see Fig. 1. The corrosion attack was ranked according to five different measurables, three of them are presented in Fig. 1. These measurables are outward-growing facetted crystal growth, compact oxide scale thickness, and internal attack by secondary oxidants such as nitridation, carburisation, or chlorination. The fourth parameter is the average number of large oxide nodules on each coupon in conjunction with a local internal corrosion attack feature. The fifth parameter is the mass change of the alloys after exposure, as shown in Fig. 2. However, mass changes must be considered with caution even though the experiments were diligently conducted. This is due to the rinsing procedure as described in supplementary A5.

Fig. 2 shows all the mass change data collected for 304L and Kanthal APMT at 800 °C in carbonate and chloride melts. No comparable mass change data for the nitrates' exposures will be reported here because the samples were only partially immersed in nitrate melts (see supplementary A4).

Exposures to carbonate melts caused mass gains for 304L and Kanthal APMT. The mass change trends indicated with dashed trendlines must be considered with the utmost caution due to the intense handling of the samples, i.e., quenching, rinsing, and drying after exposure. However, few assumptions will be made based on the mass change data in the context of our overall data collection. Kanthal APMT had a much lower mass gain, and the overall mass gain trendline also reflects sub-parabolicity. The last measurement after 1000 h, however, deviates from the indicated curve. A change in oxide morphology was found, which indicates a difference in aluminium consumption, as discussed in Section 3.2.2. Alloy 304L maintained steady-state behaviour after a fast-initial mass gain. Indications of a rapid corrosion-dissolution process supported by the steady-state progression of the mass change curve will be reported in Section 3.2.1.

Exposure to chloride melts, on the other hand, caused accelerating mass loss behaviour for both alloys. This behaviour was slower for Kanthal APMT samples. Exposure to chloride melts was the only environment in which a clear loss in sample thickness was found, cf. supplementary section B.

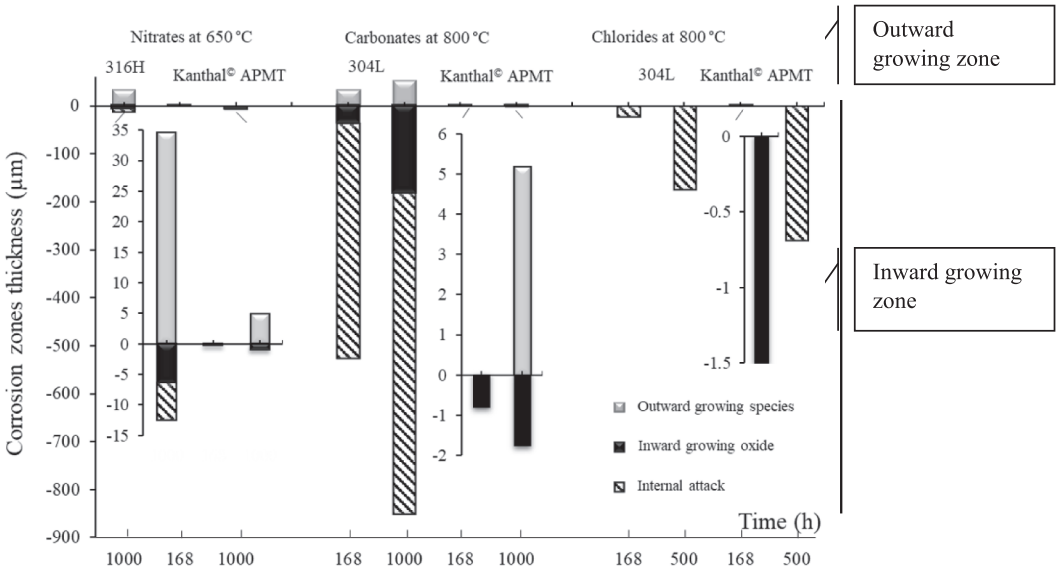

Fig. 1. Comparative schematic for all corrosion layer thickness measurements in this study. The differences between outward-growing and inward-growing species are distinguished. The horizontal axis is placed at the apparent initial material surface, where corrosion layer thickness equals zero.

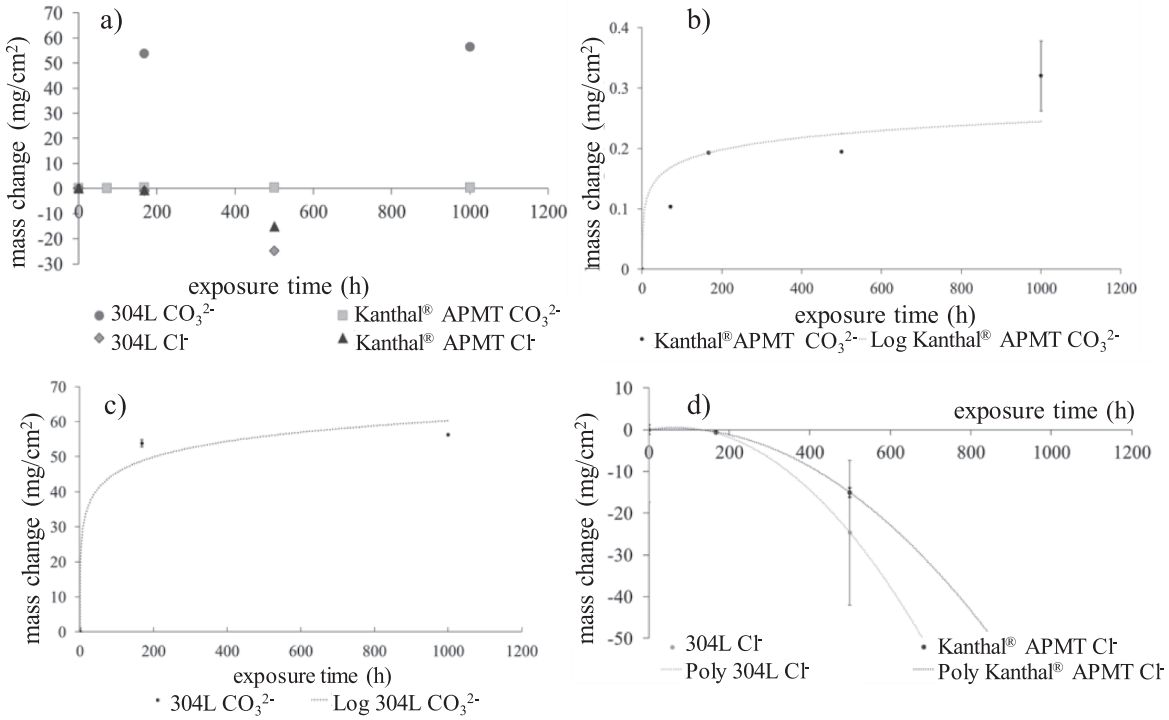

Fig. 2. a) Mass change plot for 304L and Kanthal® APMT in carbonate and chloride melts at 800 °C, (without error bars), b) mass gain of Kanthal® APMT in carbonates and trendline, c) mass gain of alloy 304L in carbonates and trendline, d) mass loss of 304L and Kanthal® APMT in chlorides and trendline. Different scales must be taken into consideration. b)-d) show error bars indicating the minimum and maximum around the plotted average value.

3.1. Corrosion performance of the alloys in solar salt

We will discuss the results from alloys exposed to the commercially used Solar Salt blend in this section. A comparison of the time-evolution of XRD spectra for stainless steel 316H and Kanthal APMT, see Fig. 3, shows that no alloy-specific signal was detectable after 168 h for the 316H stainless steel, while this signal was present for Kanthal APMT, indicating the presence of a thin alumina scale at the surface of Kanthal APMT.

The diffraction pattern observed for alloy 316H after one week exposure in Solar Salt confirms the presence of sodium ferrite species, which is in agreement with prior publications (Kruizenga and Gill, 2014; Tzvetkoff and Kolchakov, 2004; Soleimani Dorcheh et al., 2016; Fernández et al., 2015a).

After exposure, Kanthal APMT presented sodium aluminates and sodium ferrites. Corresponding potassium containing species were absent for both alloys.

3.1.1. Microstructural evolution of alloy 316H in solar salt at 650 °C

In this chapter, we discuss a metallographic cross-section of alloy 316H after 1000 h exposure in Solar Salt. Electron backscatter images and element maps, presented in Fig. 4, reveal the presence of four zones: i) a thick sodium ferrite scale with an average thickness of 40 µm. ii) an intersecting oxide zone enriched in manganese and nickel, iii) a chromium rich metal oxide interface iv) internal attack consisting of chromium nitride vail. The chromium enrichment is an attempt of the alloy to form a protective chromia scale. However, this attempt fails, which is evident when the precipitates in the suboxide region are analysed. Severe chromium depletion and chromium capture by the formation of chromium nitride render the overall performance of the oxide scale as

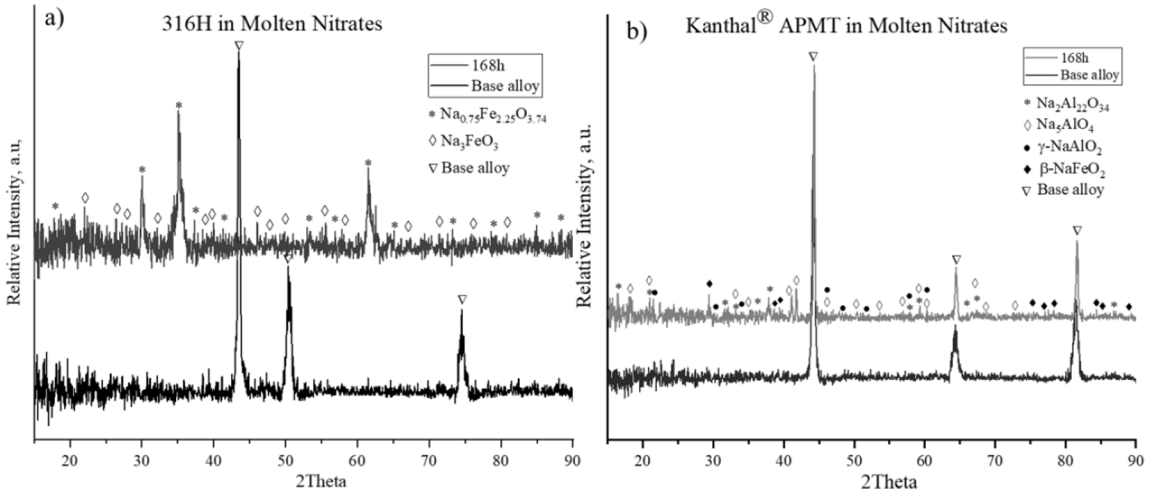

Fig. 3. XRD pattern for a) alloy 316H and b) Kanthal® APMT exposed to molten nitrate salt mixture at 650 °C for 168 h.

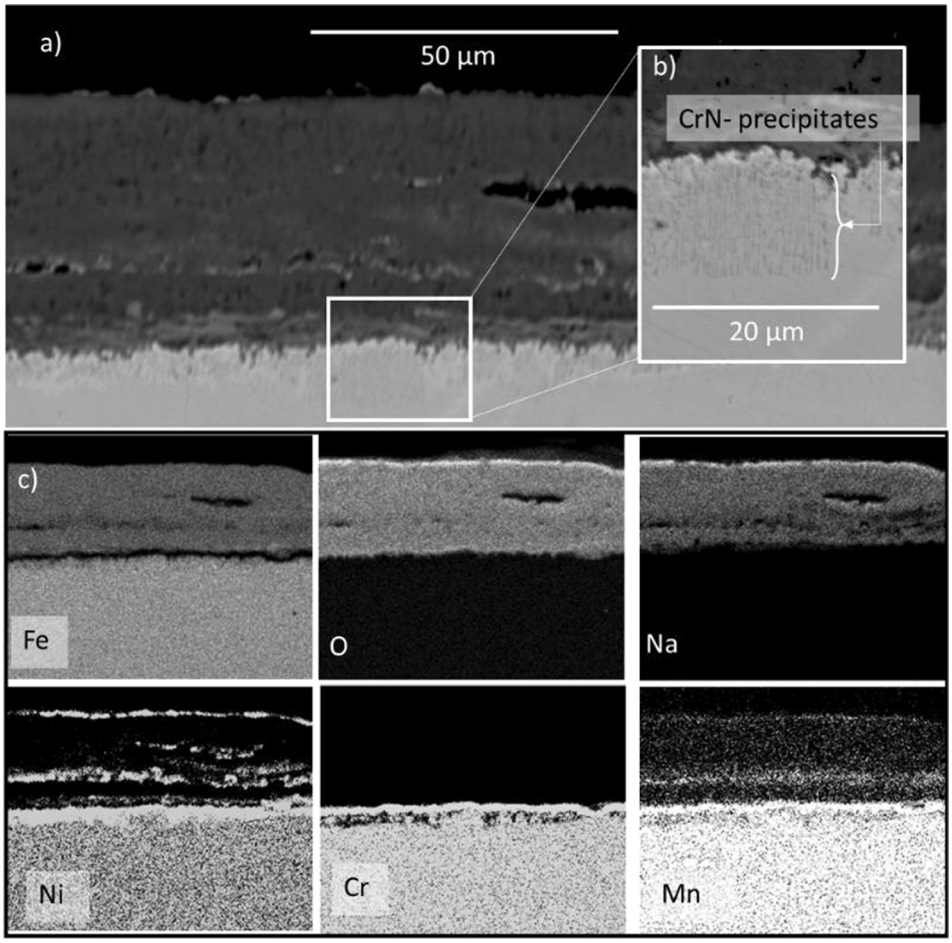

Fig. 4. a) Backscatter electron image of an alloy 316H cross section after 1000 h exposure to Solar Salt. b) Higher magnification of the suboxide zone highlighted in image a). c) Element maps of the oxide scale corresponding to image a).

non-protective. Alloy 316H developed a 7 µm thick chromia scale after exposure to Solar Salt for 1000 h at 650 °C. Alkali ferrite crystals grew rapidly outwards (25 µm average) on this sample. Internal nitridation with an average thickness of 6 µm was detected beneath the oxide layer.

3.1.2. Microstructural evolution of alloy Kanthal APMT in solar salt at 650 °C

In strong contrast to the 316H results, Kanthal APMT showed good corrosion resistance to Solar Salt at 650 °C for 168 h and 1000 h. In Fig. 5., Kanthal APMT samples show smooth sodium aluminate scales at the surface and locally occurring nodule formation that was identified as sodium ferrite, in agreement with the species identified in the XRD spectra, Fig. 3.

An underlying alumina scale beneath scars sodium ferrite nodules indicates an early stage of sodium ferrite formation and inability for further growth of those nodules.

Internal nitridation, as found for 316H, was not detected in Kanthal APMT samples. This fact is crucial, since any direct contact of alkali nitrates with the alloy or the formation of a nitrogen-permeable oxide should be prevented.

Any nitrogen ingress into the FeCrAl alloy drains the aluminium activity by the formation of thermodynamically stable AlN precipitates, until undergoing a critical concentration sustaining oxide scale growth, cf. Appendix B Table B1 Eq. 1, 4, and 5. In case a defect occurs during sodium aluminate formation, Eq. 1, internal precipitation will form aluminium nitride, Eq.4, over chromium nitride, Eq.5.

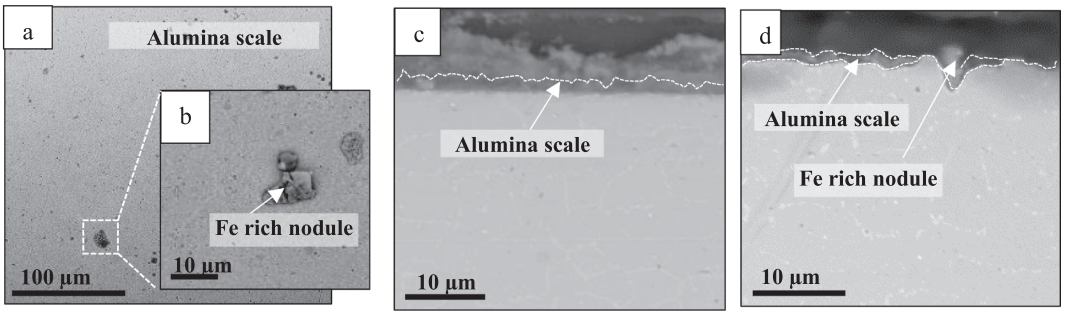

Fig. 5. Backscatter electron images of Kanthal® APMT samples after exposure to solar salt. a) and b) top view after 168 h. Cross section after c) 168 h and d) 1000 h.

3.2. Corrosion performance of the alloys in alkali carbonate melt

XRD spectra for the surfaces of alloy 304L and Kanthal APMT samples and their time-dependent evolution are shown in Fig. 6 a and b. Note that XRD was the only method used to detect lithium species in the corrosion products.

The alloy signal from the 304L sample was no longer detectable after one week of exposure at 800 °C. Spectra for the 304L sample indicate spinel oxide and lithiated oxide species, as reported in previous studies (Cruchley et al., 2016; Sah et al., 2018). Kanthal APMT, on the other hand, maintained its alloy signal for at least 1000 h, indicating a significantly thinner and slow growing oxide scale. Interestingly, after 168 h the α-lithium aluminate signal initially found on the Kanthal APMT surfaces was accompanied by a γ-lithium aluminate signal after 1000 h of exposure.

3.2.1. Microstructural evolution of alloy 304L in 33 wt% Li_2CO_3 -32 wt% Na_2CO_3- 34 wt% K_2CO_3 at 800 °C

Key images are summarised in Fig. 7, including top view images and cross sections of alloy 304L exposed for 168 h and 1000 h at 800 °C in molten carbonates. The surface morphology of the 304L sample was similar after both exposure times; the alloy surface was completely covered by rapidly growing octahedral crystallites. This finding is in agreement with the literature (Attia et al., 2002; Sarvghad et al., 2017). Lithium ferrite crystals rapidly grew with time on the surface of the 304L samples: from 33 μm after 168 h to 52 μm after 1000 h on average. Li-containing corrosion products were expected to form, based on the basicity of alkali carbonates (Spiegel et al., 1997; Evans et al., 1977) and correlate well with the spectra in Fig. 6a. Sodium and potassium corrosion species were not identified in said spectra. One critical question is whether the carbon dioxide gas environment provides sufficient oxidation potential to oxidise metallic iron. Based on reaction energy calculations, the formation of $LiFeO_2$ was found exotherm, while $NaFeO_2$ was endotherm, this explains the absence of $NaFeO_2$ in the corrosion products (supplementary data C, Table C2 Eq. 7 and 8).

Underneath the alkali ferrite crystals, a multi-layer oxide scale was revealed, which is in agreement with previous studies (Attia et al., 2002; Sarvghad et al., 2017).

The internal oxide scale propagated more rapidly than the outer crystallite scale. This zone evidently grew linear with time, since its thickness increased from 35 μm to 180 μm by prolonging the exposure time by a factor of six. The internal oxidation zone's chemistry is heterogeneous, as can be seen in the Z-contrast in the electron backscatter images in Fig. 7. EDX spot analysis identified the darkest contrast as chromium-rich iron-chromium spinel. The medium shades contain mainly iron oxide, and the brightest spots contain high nickel fractions. None of the oxides offered protection; both of the oxide species allowed oxygen and carbon to permeate into the alloy causing carburisation ($Cr_{23}C_6$) beyond the internal oxidation zone, as shown in Fig. 7d and g. Based on the SEM/EDX analysis, the internal attack in form of carbide precipitation has reached a depth of ~490 μm after 168 h and throughout the sample after 1000 h.

The precipitation of chromium carbides drains chromium activity from the alloy, inhibiting outward diffusion towards the metal/oxide interface to contribute to the formation of a protective oxide scale. Chromium carbide precipitates also lead to changes in the microstructure and mechanical properties of the alloy.

Severe internal oxidation and carburisation would point towards a significant mass gain over time. On the contrary, mass gain appears stagnant in the plot Fig. 2c. One reason could be a substantial mass loss due to the dissolution of metal ions into the carbonate melt as indicated by the melts' colouring. Chromia reacts exothermically with lithium carbonate and carbon dioxide to form liquid hexavalent lithium chromate (see Appendix B) at 800 °C (Encinas-Sánchez et al., 2018).

Alloy 304L was doubly compromised in its ability to form a protective chromium-rich oxide scale by a severe internal attack via carburisation and the dissolution of hexavalent species into the carbonate melt.

3.2.2. Microstructural evolution of Kanthal APMT in 32.1 wt% Li_2CO_3 -33.4 wt% Na_2CO_3- 34.5 wt% K_2CO_3 at 800 °C

Kanthal APMT shows very different top view features in Fig. 8 compared to the 304L sample in Fig. 7. After 168 h exposure, a smooth surface with very small $LiAlO_2$ crystallites emerged (Fig. 8a). The reaction of aluminium and chromium with sodium and lithium carbonates is spontaneous. Among these reactions, lithium aluminate has the highest exothermicity (Appendix B Table B2 Eq. 9 to 11).

After 1000 h, some significantly larger crystallites became locally visible see Fig. 8b. These crystals were identified as γ-$LiAlO_2$ as shown in Fig. 6b.

While after 168 h exposure, only one lithium aluminate phase, α-$LiAlO_2$, was detected (Fig. 6b), a second phase, γ-$LiAlO_2$, emerged after 1000 h of exposure, simultaneously with the appearance of large prismatic crystals. Several studies have been published on the thermal physical properties of the two lithium aluminate polymorphs (Danek et al., 2004; Heo et al., 2017; Bennett et al., 2003; Choi et al., 2010). α-$LiAlO_2$ is stable up to ~747–777 °C before the $\alpha \rightarrow \gamma$- $LiAlO_2$ phase

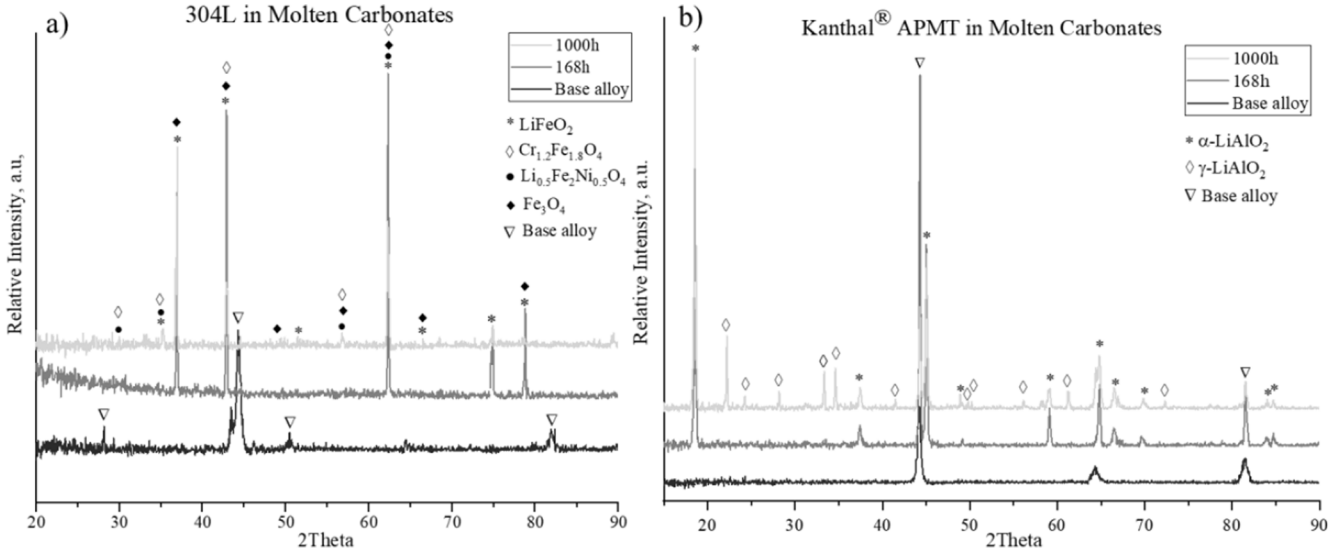

Fig. 6. XRD pattern of a) 304L and b) Kanthal® APMT after exposure to alkali carbonates at 800 °C for 168 h and 1000 h.

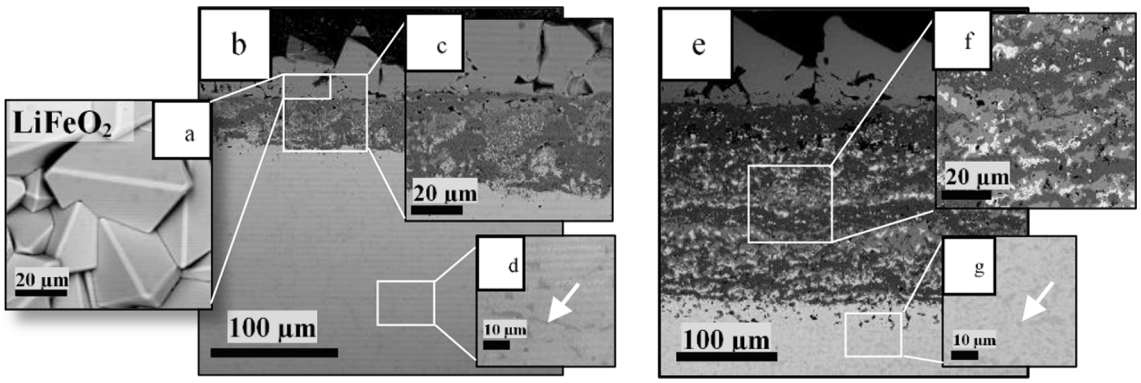

Fig. 7. a) SEM surface morphology of 304L alloy exposed to carbonate melt at 800 °C for 168 h, b) SEM cross section of 304L alloy exposed to carbonate melt at 800 °C for b) 168 h and e) for 1000 h. Higher magnification cross section shows: the internal oxidation zone for c) 168 h and f) 1000 h, and chromium carbide precipitates for d) 168 h and g) 1000 h.

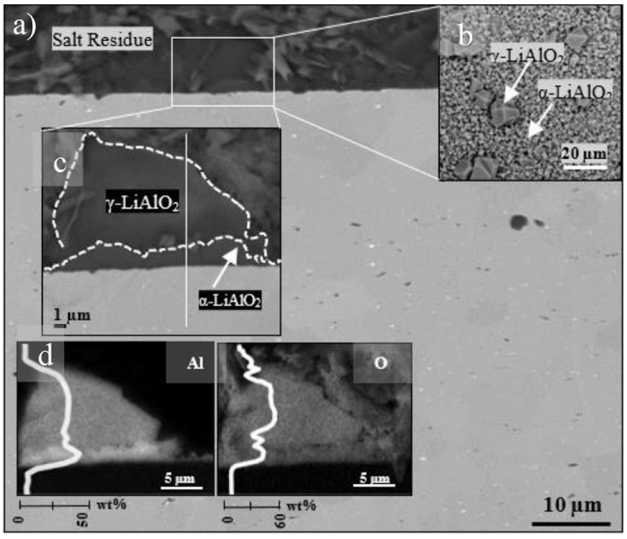

Fig. 8. a) Overview backscatter electron image of a Kanthal® APMT cross section exposed to molten carbonate salt mixture at 800 °C for 1000 h, b) top view image of the surface, c) higher magnification of the cross section, d) aluminum and oxygen element maps of position c) and corresponding lines cans.

transformation occurs. This transformation depends on different parameters e.g., operating temperature, environment, and exposure time. The transformation of α-$LiAlO_2$ to γ-$LiAlO_2$ may affect the corrosion resistivity of an alloy. Small α- $LiAlO_2$ crystallites form a protective film, while γ-$LiAlO_2$ grows large individual crystals (Heo et al., 2017). This feature renders the α- to γ-$LiAlO_2$ phase transformation undesirable. This transformation may also explain the larger window of uncertainty for the last mass change measurements after 1000 h in Fig. 2b. These measurements indicate an accelerating oxidation process.

The overall mass gain of Kanthal APMT was reduced by two magnitudes, compared to 304L, and no aluminium had been dissolved from the alloy into the melt after 1000 h. However, the overall impact of the phase transformation must be considered in long-term assessments.

Cross-section analysis was performed to test for an internal attack coinciding with the different lithium aluminate morphologies, Fig. 8c and 8d. The sample exposed for 168 h succeeded in forming a uniform, thin, and dense α-$LiAlO_2$ scale, with a thickness in the range of 0.5–3.2 µm. The α-$LiAlO_2$ scale thickness increased slightly after 1000 h, but the second morphology, γ-$LiAlO_2$, nucleated and formed larger crystals (about 6 µm high) on top of the underlying α-$LiAlO_2$ scale. Additional EDX element maps clearly show the transition front between the two aluminate morphologies. An additional line scan showed no aluminium depletion zone in the alloy's subsurface, for at least 1000 h exposure, and no indication of any internal attack.

3.3. Corrosion performance of the alloys in magnesium potassium chlorides at 800 °C

A comparison of the XRD spectra for the stainless steel 304L and Kanthal APMT after different exposure times are shown in Fig. 9. The only detectable corrosion species on 304L was magnesium oxide. $MgAl_2O_4$ and traces of a MgCrAl spinel oxide were found on Kanthal APMT. No metal chlorides were identified via XRD.

Oxidation reactions in molten chlorides are limited by the impurity oxygen in the argon gas and the residual humidity in the salt, see supplementary A2 and A3 on common impurities. Only oxides with very high thermodynamic stability can form under such extreme conditions, other species dissolve into the chloride melt. Magnesium oxide and magnesium aluminate are such stable species (Ellingham, 1944).

Furthermore, the XRD spectra for the exposed Kanthal APMT had clear signals for a molybdenum-rich intermetallic phase, a so called Laves phase. The position and role of the Laves phase will be discussed more specifically in Section 3.3.2.

The mass change data in Fig. 2 indicates that both alloys underwent accelerating mass loss, more for 304L than for Kanthal APMT. Also, the overall coupon thickness decreased as documented in the supplementary B. The dissolution processes of alloy elements is anticipated, in agreement with previously published data (Ding, W.J. et al., 2019).

3.3.1. Microstructural evolution of alloy 304L in 65 wt% KCl- 35% wt% MgCl2 at 800 °C

Alloy 304L underwent immediate leaching of alloy species by the salt. Residual humidity in the salt can only stabilise magnesium oxide originating from the melt. After 168 h of exposure a thin MgO film was found on the 304L surface (Fig. 10). Alloy species, i.e., chromium, nickel, and iron, were detected in salt particles on top of the sample as shown in EDX maps (Fig. 10b). The loss of chromium into chloride melts has also been reported by Ding et al. (Liu et al., 2016; Ding et al., 2018b). Cavities reaching ~10 µm deep int the alloy's microstructure after 168 h, formed where metals have been leached into the melt. In return, these cavities were found filled with magnesium oxide. A deep and easily distinguishable depletion zone had formed after 500 h as shown in the Chromium EDX map in Fig. 10e. This zone reached several hundred µm into the alloy and contained only about 2% chromium (see line-scan Fig. 10e). Cavities within the depletion zone, filled with magnesium oxide, and traces of chlorides, were found more than 150 µm into the alloy. Similar results have been reported by Ding et al. (2018b).

Humidity has been identified as an impurity with the highest

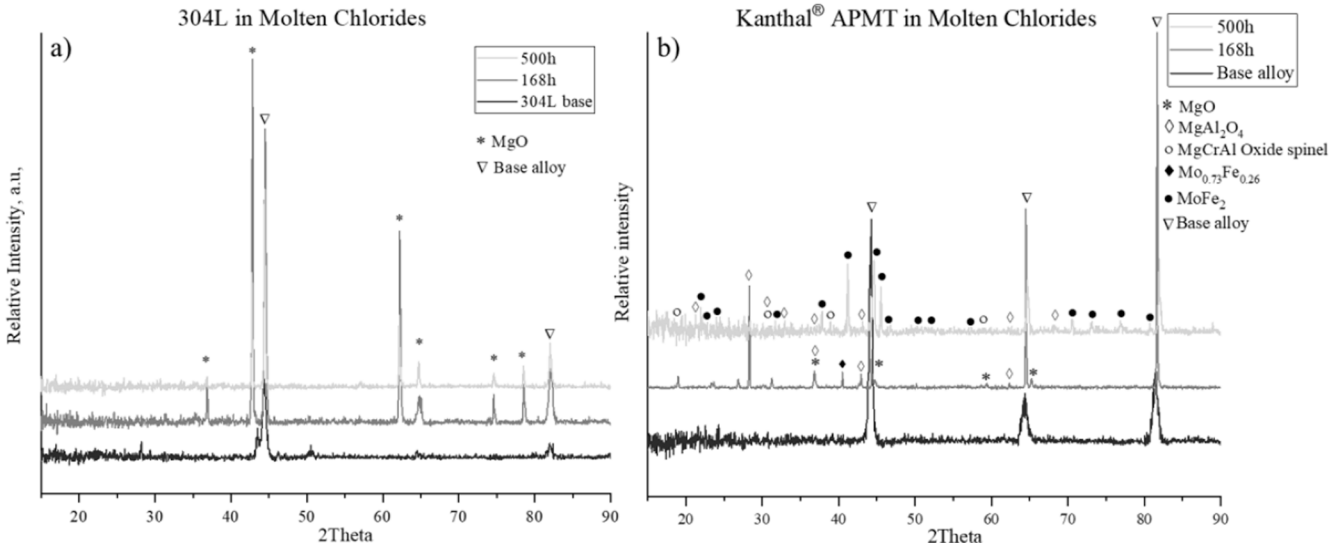

Fig. 9. XRD patterns for a) 304L and b) Kanthal® APMT alloy exposed to chloride melts at 800 °C for 168 h and 500 h.

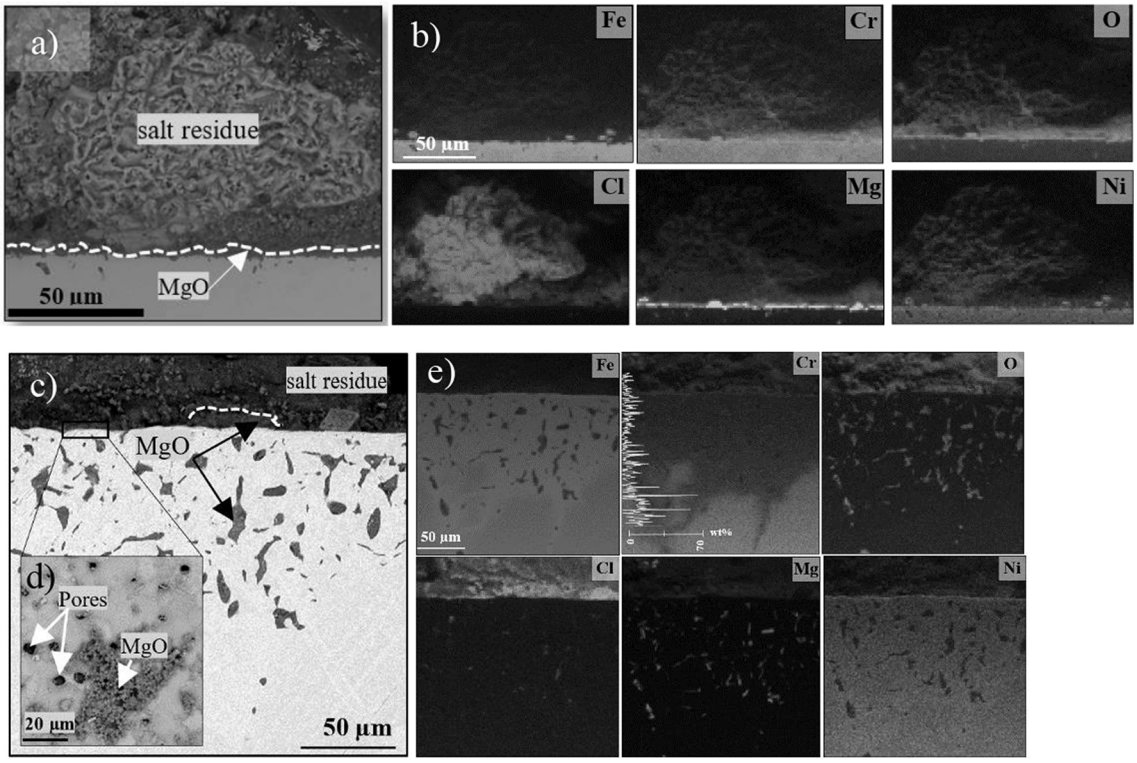

Fig. 10. Alloy 304L cross section after exposure to molten chlorides at 800 °C for a) 168 and c) 500 h, and corresponding EDX element maps b) and e). The chromium element map in e) is extended by a line scan to highlight chromium depletion. The higher magnification in the top view image d) shows magnesium oxide and pores distributed over the surface of the sample.

acceleration effect on the corrosion of stainless steels (Tian and Zhao, 2013; Ge et al., 2018; Copson, 1953; Ding et al., 2019c). Despite the additional drying sequence for the salts in inert gas prior to exposure, the impact of remaining humidity has proven substantial. This must be taken into account when considering the dimensions of the several thousand tons of salt required for a thermal storage reservoir in a CSP. Humidity control is a major economic factor.

3.3.2. Microstructural evolution of alloy Kanthal APMT in 64.41 wt% KCl-35.59% wt% $MgCl_2$ at 800 °C

Besides the $MgAl_2O$ identified via XRD, alumina particles were found by EDX top-view spot analysis (Fig. 11a).

Fig. 11b shows a bright Z-contrast in the subsurface region. Interestingly, this bright contrast was caused by molybdenum enrichment. This enrichment was sufficient to stabilise Laves phase precipitates.

The stability of the Laves phase is discussed thermodynamically in supplementary D. The thermodynamic calculations confirm a two-phase regime at 800 °C comprising BCC and C14 Laves phase with the approximate composition $(Fe_{0.75}Cr_{0.25})_2Mo$.

No internal attack was detected after 168 h.

After 500 h, however, the chloride melt compromised the alloy integrity by selectively leaching aluminium, creating a cavity network to

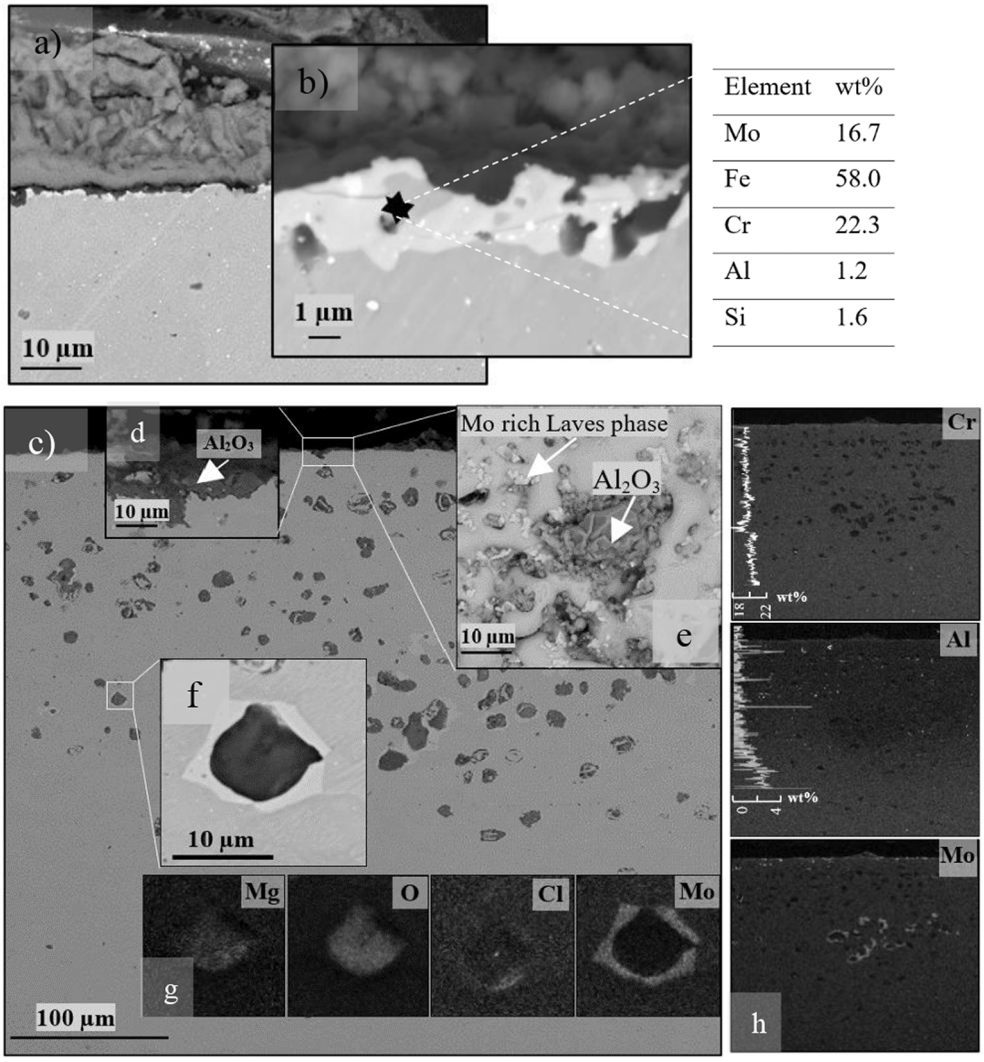

Element	wt%
Mo	16.7
Fe	58.0
Cr	22.3
Al	1.2
Si	1.6

Fig. 11. Kanthal® APMT cross section after exposure to molten chlorides at 800 °C for a) 168 and c) 500 h, and corresponding EDX element maps b) and g, h). The aluminum and chromium element maps in h) were extended with line scans to highlight aluminum depletion and the lower degree of chromium leaching. The higher magnification in the top view image e) shows magnesium oxide and pores distributed over the surface. The higher magnification cross section in d) shows a fragment of alumina scale remaining at the surface. f) shows Laves phase rims around voids.

a depth of 280 µm. Only fragments of alumina remained at the surface. The bare alloy and a pattern of pores was present at the surface. A deep-reaching depletion of aluminium was found in a cross-section analysis of the attacked material, see line scan in Fig. 11h. The remaining cavities were filled with magnesium oxide and chlorides. Aluminium leached most efficiently through the cavity network, leaving a molybdenum rich Laves phase rim around several individual cavities. After 500 h, such Laves phase rims around cavities are measured at the minimum distance of ~100 µm from the metal/salt interface. Therefore, it can be concluded that the Laves phase precipitates were transient in the overall leaching process and had already been dissolved in the upper region of the sample.

The overall mass loss for Kanthal APMT was lower than that for 304L. This was due to the lower degree of chromium leaching found for Kanthal APMT, however, the internal attack progressed deeper, compromising the integrity of the alloy.

In a previous exposure study by Gomez-Vidal *et al.*, Kanthal APMT was pre-oxidised before being brought into contact with the chloride melt. This procedure did not result in Laves phase precipitates (Gomez-Vidal et al., 2017b).

4. Conclusions

Three eutectic melts that are currently under consideration for heat transfer fluid or a thermal energy storage medium, alkali nitrates, alkali carbonates, and chlorides were brought into contact with the stainless-steel alloy 304L or 316H and Kanthal APMT.

Aspects of oxidation, dissolution, and internal attack on the alloys were systematically compared.

Material degradation in contact with alkali nitrates was comparatively slow for the stainless steel and Kanthal APMT, which was anticipated because of the lower exposure temperature. It should, however, be noted that the stainless steel underwent gradual oxide scale growth, and nitrogen permeated into the bulk alloy, which caused chromium nitride precipitation in 316H alloy. This in turn significantly lowered the chromium activity of the alloy. Internal nitride precipitation, however, is not as severe as carburisation that occurs on alloy 304L in an alkali carbonates melt. Carbide precipitation reached several hundreds of micrometres deeper into the bulk alloy after the same exposure times, which altered the overall chemistry. Kanthal APMT, on the other hand, remained nearly unaffected when exposed to carbonates or to nitrates and did not suffer from an internal attack. However, under the influence of lithium ions from the carbonates melt, a slow conversion from the film-growing α-$LiAlO_2$ to the locally growing larger γ-$LiAlO_2$ crystallites occurred, and the long-term effect of this on aluminium consumption needs further evaluation. No internal scarburisation was observed for at least 1000 h.

Chlorides melt leached elements from both 304L and Kanthal APMT. Chromium and nickel were gradually leached from the stainless-steel alloy 304L into the melt, and the resulting cavities in the

microstructure were filled with melt components. Kanthal APMT, however, resisted severe leaching of alloy elements during the first 168 h by forming magnesium aluminate on the sample surface. This resistance broke down after 500 h, resulting in the rapid leaching of aluminium, which reached deeper in Kanthal APMT than the depth of chromium leaching found for alloy 304L. Cavities created by the leaching were filled with magnesium oxide and chloride surrounded by a $(Fe_{0.75}Cr_{0.25})_2Mo$ Laves phase, indicating that molybdenum leached much slower than chromium and aluminium. Laves phase rims seemed to prevent Kanthal APMT from rapid chromium leaching, compared to alloy 304L, thus explaining the overall lower mass loss measured for Kanthal APMT.

The overall conclusion is that nitrates are the best choice as a calculated risk, since even the stainless steel that suffered an internal attack reacted comparably slow and predictably. Alkali carbonates degraded the stainless steel unacceptably fast through carburisation. Kanthal APMT is a very good alternative in this case provided that the α- to γ-transition of $LiAlO_2$ is slow and does not lead to any aluminium depletion for at least 1000 h. Chloride melts were detrimental to both alloys investigated. However, molybdenum proved to be a possible influencing element. Molybdenum formed a Laves phase barrier to chromium leaching, which however, did not prevent the rapid dissolution of aluminium from the alloy.

Declaration of Competing Interest

The authors declare that they have no known competing financial interests or personal relationships that could have appeared to influence the work reported in this paper.

Acknowledgments

This work was financially supported by Vinnova within the ALSTEr Project as part of the Jernkontoret initiative Metalliska Material. The Swedish Energy Agency continues to financially support our efforts within the thermal storage for SOLEL initiative under contract number 44653-1 (Jan-Erik Svensson) and as a partner in the High Temperature Corrosion Competence Centre (Lars-Gunnar Johansson).

Appendix A. Supplementary data

Supplementary data to this article can be found online at https://doi.org/10.1016/j.solener.2021.06.069.

References

Attia, A.A., Salih, S.A., Baraka, A.M., 2002. Corrosion and passivation behaviors of some stainless steel alloys in molten alkali carbonates. Electrochim. Acta 48 (2), 113–118.
Bennett, M.J., Newton, R., Nicholls, J.R., 2003. The behaviour of commercial FeCrAlRE alloys in nitrogen-oxygen - water vapour bioxidant environments. Mater. High Temp. 20 (3), 347–356.
Bradshaw, R.W., Goods, S.H., 2001. Corrosion resistance of stainless steels during thermal cycling in alkali nitrate molten salts. ; Sandia National Laboratories (SNL), Albuquerque, NM, and Livermore, CA (United States), p. Medium: ED; Size: 39 p.
Bradshaw, R.W., Clift, W.M., 2010. Effect of chloride content of molten nitrate salt on corrosion of A516 carbon steel. Sandia National Laboratories, Albuquerque, New Mexico 87185 and Livermore, California 94550, pp. 1–27.
Caitlin, M., Y., S., W., C., Maclaurin, G., Turchi, C., Mehos, M., 2019. The Potential Role of Concentrating Solar Power within the Context of DOE's 2030 Solar Cost Target National Renewable Energy Laboratory, p. https://www.nrel.gov/docs/fy19osti/71912.pdf.
Cheng, W.-J., Chen, D.-J., Wang, C.-J., 2015. High-temperature corrosion of Cr–Mo steel in molten LiNO3–NaNO3–KNO3 eutectic salt for thermal energy storage. Sol. Energy Mater. Sol. Cells 132, 563–569.
Choi, H.J., Lee, J.J., Hyun, S.H., Lim, H.C., 2010. Phase and microstructural stability of electrolyte matrix materials for molten carbonate fuel cells. Fuel Cells 10 (4), 613–618.
Copson, H.R., 1953. Corrosion of heating electrodes in molten chloride baths. J. Electrochem. Soc. 100 (6), 257.
Cruchley, Samuel, Evans, Hugh, Taylor, Mary, 2016. An overview of the oxidation of Ni-based superalloys for turbine disc applications: surface condition, applied load and mechanical performance. Mater. High Temp. 33 (4-5), 465–475. https://doi.org/10.1080/09603409.2016.1171952.
Danek, V., Tarniowy, M., Suski, L., 2004. Kinetics of the α → γ phase transformation in LiAlO2 under various atmospheres within the 1073–1173 K temperatures range. Journal of Materials Science 39 2429–2435.
de Miguel, M.T., Encinas-Sánchez, V., Lasanta, M.I., García-Martín, G., Pérez, F.J., 2016. Corrosion resistance of HR3C to a carbonate molten salt for energy storage applications in CSP plants. Sol. Energy Mater. Sol. Cells 157, 966–972.
Ding, W., Bauer, T., 2021. Progress in research and development of molten chloride salt technology for next generation concentrated solar power plants. Engineering 7 (3), 334–347.
Ding, W., Bonk, A., Bauer, T., 2018a. Corrosion behavior of metallic alloys in molten chloride salts for thermal energy storage in concentrated solar power plants: a review. Front. Chem. Sci. Eng. 564–576.
Ding, W., Bonk, A., Bauer, T., 2019. Molten chloride salts for next generation CSP plants: Selection of promising chloride salts & study on corrosion of alloys in molten chloride salts. AIP Conference Proceedings 2126(1), 200014.
Ding, W.J., Gomez-Vidal, J., Bonk, A., Bauer, T., 2019b. Molten chloride salts for next generation CSP plants: electrolytical salt purification for reducing corrosive impurity level. Sol. Energy Mater. Sol. Cells 199, 8–15.
Ding, W., Shi, H., Xiu, Y., Bonk, A., Weisenburger, A., Jianu, A., Bauer, T., 2018b. Hot corrosion behavior of commercial alloys in thermal energy storage material of molten MgCl2/KCl/NaCl under inert atmosphere. Solar Energy Materials and Solar Cells. Elsevier B.V. 22–30.
Ding, W., Shi, H., Jianu, A., Xiu, Y., Bonk, A., Weisenburger, A., Bauer, T., 2019a. Molten chloride salts for next generation concentrated solar power plants: mitigation strategies against corrosion of structural materials. Solar Energy Materials and Solar Cells. Elsevier B.V. 298–313.
Ellingham, J.T., 1944. Transactions and communications. J. Soc. Chem. Ind. 63 (5), 125–160.
Encinas-Sánchez, V., de Miguel, M.T., García-Martín, G., Lasanta, M.I., Pérez, F.J., 2018. Corrosion resistance of Cr/Ni alloy to a molten carbonate salt at various temperatures for the next generation high-temperature CSP plants. Sol. Energy 171, 286–292.
Encinas-Sánchez, V., de Miguel, M.T., Lasanta, M.I., García-Martín, G., Pérez, F.J., 2019. Electrochemical impedance spectroscopy (EIS): An efficient technique for monitoring corrosion processes in molten salt environments in CSP applications. Sol. Energy Mater. Sol. Cells 191, 157–163.
Evans, H.E., Hilton, D.A., Holm, R.A., 1977. Internal attack during the oxidation of nitrided stainless steels. Oxid Met. 11 (1), 1–21.
Fähsing, D., Oskay, C., Meißner, T.M., Galetz, M.C., 2018. Corrosion testing of diffusion-coated steel in molten salt for concentrated solar power tower systems. Surface and Coatings Technology. Elsevier B.V. 46–55.
Fernández, A.G., Lasanta, M.I., Pérez, F.J., 2012. Molten salt corrosion of stainless steels and low-Cr steel in CSP plants. Oxid. Met. 78 (5–6), 329–348.
Fernández, A.G., Rey, A., Lasanta, I., Mato, S., Brady, M.P., Pérez, F.J., 2014. Corrosion of alumina-forming austenitic steel in molten nitrate salts by gravimetric analysis and impedance spectroscopy. Mater. Corros. 267–275.
Fernández, A.G., Cortes, M., Fuentealba, E., Pérez, F.J., 2015a. Corrosion properties of a ternary nitrate/nitrite molten salt inconcentrated solar technology. Renew. Energy 177–183.
Fernández, A.G., Galleguillos, H., Fuentealba, E., Pérez, F.J., 2015b. Corrosion of stainless steels and low-Cr steel in molten Ca(NO3)2–NaNO3–KNO3 eutectic salt for direct energy storage in CSP plants. Sol. Energy Mater. Sol. Cells 141, 7–13.
Fernández, A.G., Pineda, F., Walczak, M., Cabeza, L.F., 2019. Corrosion evaluation of alumina-forming alloys in carbonate molten salt for CSP plants. Renew. Energy 140, 227–233.
Frangini, S., Loreti, S., 2006. The role of temperature on the corrosion and passivation of type 310S stainless steel in eutectic (Li + K) carbonate melt. J. Power Sources 800–804.
Ge, Z., Huang, Y., Ding, Y., 2018. Eutectic composition-dependence of latent heat of binary carbonates (Na2CO3/Li2CO3). Sol. Energy Mater. Sol. Cells 179, 202–206.
Gomes, A., Navas, M., Uranga, N., Paiva, T., Figueira, I., Diamantino, T.C., 2019. High-temperature corrosion performance of austenitic stainless steels type AISI 316L and AISI 321H, in molten Solar Salt. Solar Energy. Elsevier 408–419.
Gomez-Vidal, J.C., Tirawat, R., 2016. Corrosion of alloys in a chloride molten salt (NaCl-LiCl) for solar thermal technologies. Solar Energy Materials and Solar Cells. Elsevier 234–244.
Gomez-Vidal, J.C., Noel, J., Weber, J., 2016. Corrosion evaluation of alloys and MCrAlX coatings in molten carbonates for thermal solar applications. Solar Energy Materials and Solar Cells. Elsevier 517–525.
Gomez-Vidal, J.C., Fernandez, A.G., Tirawat, R., Turchi, C., Huddleston, W., 2017a. Corrosion resistance of alumina-forming alloys against molten chlorides for energy production. I: Pre-oxidation treatment and isothermal corrosion tests. Sol. Energy Mater. Sol. Cells 166, 222–233. https://doi.org/10.1016/j.solmat.2017.02.019.
Gomez-Vidal, J.C., Fernandez, A.G., Tirawat, R., Turchi, C., Huddleston, W., 2017b. Corrosion resistance of alumina forming alloys against molten chlorides for energy production. II: Electrochemical impedance spectroscopy under thermal cycling conditions. Sol. Energy Mater. Sol. Cells 166, 234–245.
Goods, S.H., Bradshaw, R.W., 2004. Corrosion of stainless steels and carbon steel by molten mixtures of commercial nitrate salts. J. Mater. Eng. Perform. 13 (1), 78–87.
Goods, S.H., Bradshaw, R.W., Prairie, M.R., Chavez, J.M., 1994. Corrosion of stainless and carbon steels in molten mixtures of industrial nitrates. Sandia National Lab. (SNL-CA), Livermore, CA (United States), 37 p.

Grosu, Y., Bondarchuk, O., Faik, A., 2018. The effect of humidity, impurities and initial state on the corrosion of carbon and stainless steels in molten HitecXL salt for CSP application. Sol. Energy Mater. Sol. Cells 174, 34–41.
Heo, S.J., Hu, B., Uddin, M.A., Aphale, A., Hilmi, A., Yuh, C.-Y., Surendranath, A., Singh, P., 2017. Role of exposure atmospheres on particle coarsening and phase transformation of LiAlO2. J. Electrochem. Soc. 164 (8), H5086–H5092.
Ho, C.K., Carlson, M., Garg, P., Kumar, P., 2016. Technoeconomic analysis of alternative solarized s-CO2 brayton cycle configurations. J. Sol. Energy Eng. 138 (5).
Hofmeister, M., Klein, L., Miran, H., Rettig, R., Virtanen, S., Singer, R.F., 2015. Corrosion behaviour of stainless steels and a single crystal superalloy in a ternary LiCl–KCl–CsCl molten salt. Corros. Sci. 90, 46–53.
IEA, 2010. Technology Roadmap - Concentrating Solar Power, IEA, Paris https://www.iea.org/reports/technology-roadmap-concentrating-solar-power.
Kruizenga, A., Gill, D., 2014. Corrosion of iron stainless steels in molten nitrate salt. Energy Procedia 49, 878–887.
Li, C.-j., Li, P., Wang, K., Molina, E.E., 2014. Survey of Properties of Key Single and Mixture Halide Salts for Potential Application as High Temperature Heat Transfer Fluids for Concentrated Solar Thermal Power Systems. pp. 133-157.
Li, H., Yang, X., Yin, X., Wang, X., Tang, J., Gong, J., 2021. Effect of chloride impurity on corrosion kinetics of stainless steels in molten solar salt for CSP application: experiments and modeling. Oxid. Met. 95 (3–4), 311–332.
Liu, M., Steven Tay, N.H., Bell, S., Belusko, M., Jacob, R., Will, G., Saman, W., Bruno, F., 2016. Review on concentrating solar power plants and new developments in high temperature thermal energy storage technologies. Renewable and Sustainable Energy Reviews. Elsevier 1411–1432.
Mehos, M., Turchi, C., Vidal, J., Wagner, M., Ma, Z., Ho, C., Kolb, W., Andraka, C., Kruizenga, A., 2017. Concentrating Solar Power Gen3 Demonstration Roadmap. National Renewable Energy Lab. (NREL), Golden, CO (United States), 140 p.
Meißner, T.M., Oskay, C., Bonk, A., Grégoire, B., Donchev, A., Solimani, A., Galetz, M.C., 2021. Improving the corrosion resistance of ferritic-martensitic steels at 600 °C in molten solar salt via diffusion coatings. Solar Energy Materials and Solar Cells 227.
Ni, C.S., Lu, L.Y., Zeng, C.L., Niu, Y., 2011. Electrochemical impedance studies of the initial-stage corrosion of 310S stainless steel beneath thin film of molten (0.62Li,0.38K)2CO3 at 650°C. Corros. Sci. 53 (3), 1018–1024.
Palacios, A., Navarro, M.E., Jiang, Z., Avila, A., Qiao, G., Mura, E., Ding, Y., 2020. High-temperature corrosion behaviour of metal alloys in commercial molten salts. Sol. Energy 201, 437–452.
Phillips, W., Karmiol, Z., Chidambaram, D., 2019. Effect of Metallic Li on the Corrosion Behavior of Inconel 625 in Molten LiCl-Li 2 O-Li Journal of The Electrochemical Society. pp. C162-C168.
Prieto, C., Fereres, S., Ruiz-Cabañas, F.J., Rodriguez-Sanchez, A., Montero, C., 2020. Carbonate molten salt solar thermal pilot facility: plant design, commissioning and operation up to 700 °C. Renew. Energy 151, 528–541.
Ravi Shankar, A., Mathiya, S., Thyagarajan, K., Kamachi Mudali, U., 2010. Corrosion and microstructure correlation in molten LiCl-KCl medium. Metall. Mater. Trans. A 41 (7), 1815–1825.
Sah, S.P., Tada, E., Nishikata, A., 2018. Corrosion behaviour of austenitic stainless steels in carbonate melt at 923 K under controlled CO2-O2 environment. Corrosion Science. Elsevier Ltd 310–317.
Sarvghad, M., Steinberg, T.A., Will, G., 2017. Corrosion of steel alloys in eutectic NaCl+ Na2CO3 at 700 °C and Li2CO3 + K2CO3 + Na2CO3 at 450 °C for thermal energy storage. Sol. Energy Mater. Sol. Cells 170, 48–59.
Sarvghad, M., Delkasar Maher, S., Collard, D., Tassan, M., Will, G., Steinberg, T.A., 2018a. Materials compatibility for the next generation of Concentrated Solar Power plants. Energy Storage Mater. 179–198.
Sarvghad, M., Steinberg, T.A., Will, G., 2018b. Corrosion of stainless steel 316 in eutectic molten salts for thermal energy storage. Sol. Energy 198–203.
Selman, M.S.Y.a.J.R., 1999. Oxidation-lithiation of nickel, iron and cobalt in contact with molten carbonate. Solid State Ionics 124(1), 149–160.
Soleimani Dorcheh, A., Durham, R.N., Galetz, M.C., 2016. Corrosion behavior of stainless and low-chromium steels and IN625 in molten nitrate salts at 600 °C. Solar Energy Materials and Solar Cells. Elsevier 109–116.
Spiegel, M., Biedenkopf, P., Grabke, H.J., 1997. Corrosion of iron base alloys and high alloy steels in the Li2CO3-K2CO3 eutectic mixture. Corros. Sci. 39 (7), 1193–1210.
Steinmann, W.D., 2015. Thermal energy storage systems for concentrating solar power (CSP) technology. Adv. Therm. Energy Storage Syst. 511–531.
Tian, Y., Zhao, C.Y., 2013. A review of solar collectors and thermal energy storage in solar thermal applications. Appl. Energy 104, 538–553.
Tzvetkoff, T., Kolchakov, J., 2004. Mechanism of growth, composition and structure of oxide films formed on ferrous alloys in molten salt electrolytes—a review. Mater. Chem. Phys. 87 (1), 201–211.
Vignarooban, K., Xu, X., Arvay, A., Hsu, K., Kannan, A.M., 2015. Heat transfer fluids for concentrating solar power systems - a review. Applied Energy. Elsevier Ltd 383–396.
Walczak, M., Pineda, F., Fernández, Á.G., Mata-Torres, C., Escobar, R.A., 2018. Materials corrosion for thermal energy storage systems in concentrated solar power plants. Renew. Sustain. Energy Rev. 86, 22–44.
Wu, Y.-T., Ren, N., Wang, T., Ma, C.-F., 2011. Experimental study on optimized composition of mixed carbonate salt for sensible heat storage in solar thermal power plant. Sol. Energy 85 (9), 1957–1966.
Yamamoto, Y., Takeyama, M., Lu, Z.P., Liu, C.T., Evans, N.D., Maziasz, P.J., Brady, M.P., 2008. Alloying effects on creep and oxidation resistance of austenitic stainless steel alloys employing intermetallic precipitates. Intermetallics 16 (3), 453–462.
Yin, J.M., Zheng, Q.Y., Peng, Z.R., Zhang, X.R., 2019. Review of supercritical CO2 power cycles integrated with CSP. Int. J. Energy Res. 44 (3), 1337–1369.
Zhao, Y., Li, P., Jin, H., 2017. Heat transfer performance comparisons of supercritical carbon dioxide and NaCl–KCl–ZnCl2 Eutectic Salts for Solar s-CO2 Brayton Cycle. Energy Procedia 142, 680–687.